1   ***Nano-textured phase coexistence in the correlated insulator V₂O₃***

2

3   A. S. McLeod[1], E. van Heumen[1,2], J. G. Ramirez[1], S. Wang[1], T. Saerbeck[1*], S. Guenon[1],

4   M. Goldflam[1], L. Anderegg[1], P. Kelly[1], A. Mueller[1], M. Liu[1**], I. K. Schuller[1], D. N.

5   Basov[1]

6   [1] University of California San Diego, 9500 Gilman Dr, La Jolla, CA 92093

7   [2] University of Amsterdam, Sciencepark 904, 1098 XH Amsterdam, Netherlands

8

9   **Abstract:**

10   While the insulator-metal transition remains among the most studied phenomena in

11   correlated electron physics, its interplay with spatially textured phase coexistence

12   at the meso- and nano-scales remains poorly explored. Here we reveal real-space

13   evolution of the low temperature insulator-metal transition in a V₂O₃ thin film

14   imaged at high spatial resolution by cryogenic near-field infrared microscopy. In

15   the vicinity of insulator-to-metal temperature (~160-180 K) we resolve

16   spontaneously nano-textured coexistence of metal and correlated (Mott) insulator

17   phases associated with percolation and an underlying structural phase transition.

18   Augmented with macroscopic temperature-dependent x-ray diffraction

19   measurements of the same film, a quantitative analysis of nano-infrared images

20   acquired across the transition suggests decoupling of electronic and structural

21   transformations. Persistent low-temperature metallicity is accompanied by

Present affiliation:
*Institut Laue-Langevin, 71 avenue des Martyrs, 38000 Grenoble, France
**Stony Brook University, Stony Brook, New York 11794, USA

22   unconventional critical behavior through the film's first-order insulator-metal

23   transition, suggestive of Coulomb frustration.

24

25   **Manuscript Text:**

26   The subtle interplay of charge, spin, and orbital degrees of freedom in

27   complex correlated oxides is known to result in strongly inhomogeneous phases[1]. In

28   several families of correlated oxides including cuprates [2,3] and manganites [4,5,6],

29   experimentally observed emergent real-space patterns provide fundamental clues

30   to the principles underlying exotic behavior of these systems. The real-space self-

31   organization of electronic phases remains largely unexplored in many classes of

32   materials exhibiting a first-order insulator-metal transition (IMT), attributable

33   mostly to the absence of real-space probes capable of imaging the highly insulating

34   side of the transition with nano-scale resolution. Enabled by nano-resolved infrared

35   (nano-IR) imaging [7], we demonstrate in this article how a self-organized real-space

36   electronic nanotexture can underly more than five orders of magnitude in increased

37   resistivity through the IMT of V_2O_3. Furthermore, we resolve hitherto unreported

38   characteristics of this correlated electron system, demonstrating that stabilized

39   phase coexistent can provide a unique window onto the interactions governing an

40   insulator-metal transition that was previously considered monolithically first-order.

41   The IMT in V_2O_3 from paramagnetic metal (PM) to low temperature ($T\sim150$

42   K) antiferromagnetic insulator (AFI) arises from thermally perturbing the delicate

43   competition between kinetic energy and mutual Coulomb repulsion among

44   conduction electrons [8,9], leading to abrupt electron localization and a 0.7 eV band-

45 gap [10]. These features appear intimately tied to a structural phase transition (SPT)

46 from a hexagonal (corundum) lattice to a lower symmetry monoclinic structure [8]. In

47 recent years, increasingly refined studies have revealed unforeseen aspects of this

48 transition [11,12,13], hypothesizing a more subtle phase diagram where real-space

49 phase inhomogeneities play an essential role. The IMT and SPT have been found to

50 decouple in the related compound VO_2, whereby a strongly correlated monoclinic

51 metal emerges between low temperature monoclinic insulating and high

52 temperature rutile metallic phases [14,15,16]. Real-space phase separation amidst this

53 IMT results in a resistive transition governed by percolation. However, the exact

54 role of Mott physics in VO_2 remains hotly debated, calling for a critical examination

55 of real-space features amidst the IMT of V_2O_3 at low-T, where a localization-

56 delocalization mechanism is more conclusively at work [9,17 18,19].

57   We developed cryogenic infrared near-field (nano-IR) imaging to assess

58 nano-scale phase inhomogeneity emerging through the classic IMT in V_2O_3.   To

59 explore phase coexistence amidst the transition, we image a high-quality V_2O_3 thin

60 film, revealing a real-space nanotexture reflective of interactions governing the IMT.

61 At temperatures of phase coexistence, our local nano-optical probe first resolves bi-

62 directional stripes of the correlated insulator phase percolating through the

63 paramagnetic metal, whereas at temperatures below the transition metallic droplets

64 persist in an otherwise insulating background. Nevertheless, macroscopic x-ray

65 diffraction (XRD) of the same film indicates a virtually complete structural phase

66 transition from corundum to monoclinic structure at these temperatures. Our nano-

67 IR imaging therefore reveals V_2O_3 can support a monoclinic metal phase.

68　　Characterization of evolving real-space correlations and critical scaling among

69　　electronic inhomogeneities suggest that Coulomb frustration may be operative in

70　　the stability of monoclinic metallicity.

71

72　　　　　Scattering-type scanning near-field optical microscopy (s-SNOM) enables

73　　sub-diffractional imaging of surface optical properties [20,7] at variable temperatures

74　　[21,22], with a resolution strictly limited only by the geometric probe sharpness. We

75　　present 25 nm-resolved images of the locally back-scattered near-field amplitude

76　　(abbreviated to *nano-IR signal*, or *S*) collected at low temperatures (Fig. 1a) by a

77　　newly developed cryogenic near-field scanning optical microscope (further details

78　　in Supplementary Information [SI] and fig. S1 and S2). The sample is a high-quality

79　　300 nm thick highly oriented V_2O_3 film (3 nm RMS surface roughness; see SI and fig.

80　　S8) grown on sapphire (Methods) that displays a five-orders of magnitude increase

81　　in electrical resistance across the IMT from 180K to 150K (Fig. 1d) with a

82　　cooling/warming hysteresis of 6K, characteristic of a first-order phase transition.

83　　We recorded nano-IR images upon cooling from room temperature across the IMT

84　　down to *T*=24 K with a temperature interval of 2-4K in the thermal window 160K -

85　　180K, followed by a similar number of measurements upon warming to room

86　　temperature. All measurements were conducted in an ultra-high vacuum ($<10^{-8}$

87　　mbar) environment to prevent surface contamination. Lithographically patterned

88　　gold pad electrodes on the film enabled *in situ* resistance measurements for

89　　accurate thermometry calibrations between nano-IR imaging and *ex situ*

90　　measurements of the same film (SI and fig. S6).

91   Throughout this work we examine images of nano-IR signal S normalized to

92   an absolute reference through inclusion of a gold electrode within the field of view

93   (FOV) (not shown; see SI and figs. S3-5 for details of nano-IR image preparation).

94   Nano-IR signals are a capable probe of local metallicity and therefore of the nano-

95   scale IMT in correlated oxides [22,14,20]. Metallic regions where the DC-conductivity is

96   high and the real part of the dielectric function is negative (at the proving IR

97   frequency) yield high nano-IR signals comparable to that of good metals (*viz.* gold).

98   Here, we apply a color scheme in which *red* represents high nano-IR signal,

99   indicating metallic regions.   In contrast, insulating domains where the dielectric

100   function is positive produce significantly reduced nano-IR signal [22,20] and are

101   represented in *blue* within our color scheme. Fig. 1c presents a subset of images

102   extracted from a spatially constant $20 \times 20 \ \mu m^2$ FOV at select temperatures through

103   a cooling and warming cycle (acquisition details in SI) measured at 920 cm^{-1} (~11

104   μm wavelength) well within the free-carrier (Drude) optical response of V_2O_3

105   resolved by far-field spectroscopy [12,10,9]. The most prominent features of these

106   images are bi-directional stripes emerging through the midst of the transition. Upon

107   cooling from the metallic state (204 K), stripes of insulating material appear (175

108   K), grow (172 K), and fragment the metallic state (169 K), producing a striped

109   pattern of metallicity. At temperatures associated with rapid growth in film

110   resistance (160-170 K), metallic stripes disconnect (164 K), disorder into droplets,

111   and subsequently vanish into an insulating background (162 K). The transition

112   follows a reverse trajectory upon heating, albeit with a 6 K hysteresis. Images

113   acquired at higher spatial resolution (25 nm pixels) are presented in Fig. 1b, clearly

114   showing the growth of metallic domains in an insulating background upon warming.

115

116   We draw several qualitative conclusions from our images. First, the IMT

117   progresses upon decreasing temperature through four successive stages: i) a

118   homogeneous metallic state, ii) a stripe-like nano-texture of percolating electronic

119   phase coexistence, iii) an inhomogeneous insulating state supporting persistent

120   metallic droplets, and iv) a final homogenous correlated insulating state. Second,

121   the bipartite character of phase coexistence suggests a first-order phase transition,

122   in accord with conventional expectations for the discontinuous Mott transition into

123   a magnetically ordered state (AFI) [9,8,23]. The majority of "domain walls" between

124   metallic and insulating regions are sharp within our spatial resolution (Fig. 1b).

125   Third, nano-IR signal levels among the distinct phases evolve gradually with

126   temperature across the transition uncovering *bona fide* thermal evolution of the

127   electronic response, in contrast to a putative "monolithic" phase transition between

128   static end-phases. Fig. 2a quantifies the *dynamically binary* character of the

129   transition through a histogram representation of nano-IR signals recorded at

130   distinct temperatures upon warming. Similar to the case of VO_2 [24], we observe that

131   each bimodal nano-IR signal distribution comprises two distinct populations amidst

132   the IMT. We identify these with "insulating" (dashed blue) and "metallic" (dashed

133   red) populations, each well fit by an asymmetric (skew) normal distribution.

134   Whereas a possible admixture of phases below our spatial resolution cannot

135   be ruled out, the marked temperature dependence of the observed "metallic phase"

136 remains consistent with continuous evolution in optical conductivity among distinct

137 and locally homogeneous phases, attributable to a suppression of quasiparticle

138 weight or pseudogap across the IMT as predicted theoretically [25] and suggested by

139 area-averaged spectroscopies [23,11,10]. Meanwhile, substantial temperature

140 dependence among "insulating" regions also invites speculation. Calculations by

141 cellular dynamical mean-field theory have proposed a narrow- to large-gap

142 progression of the Mott insulating state in the phase-coexistent regime of the

143 Hubbard model. [26] Likewise, mechanistic studies of near-field microscopy have

144 confirmed a notably non-trivial relation between optical permittivity and nano-

145 optical contrast [27], whereby a high-permittivity or narrow-gap semiconductor could

146 present a high nano-IR signal (normalized S of order 0.5) consistent with our

147 observations among these non-metallic regions for $T \gtrsim 170K$.

148   A detailed comparison with macroscopic resistivity bolsters our assignment

149 of insulating and metallic regions: at each temperature, the point of intersection for

150 the two normally distributed populations (Fig. 2a) yields a threshold nano-IR signal

151 discerning metal from insulator in a most probable sense. We apply this

152 temperature-dependent threshold S_{thresh} to assign individual pixels to populations of

153 higher or lower conductivity (*viz.* metal or insulator). Thus binarized, we identified

154 unambiguous individual electronic clusters and overall electronic phase fractions

155 from our images. The dash-dotted curves of Fig. 2b obtained by this analysis display

156 the area A_{max} (percentage of the FOV) of the largest connected *embedded-phase*

157 cluster. Fig. 2b shows that A_{max} peaks at a temperature identifiable with the

158 percolation threshold T_{perc}. At this temperature the embedding phase switches in

159   identity from "metallic" to "insulating" upon cooling, or *vice versa* upon warming.

160   T_{perc} thus marks the percolation event, *i.e.* the formation of an "infinite" conducting

161   pathway across the entire FOV and, we infer, the whole V_2O_3 film. Meanwhile, T_{perc} is

162   also identifiable from the film's temperature dependent electrical resistance R and

163   conductance $G = R^{-1}$. When viewed as an effective circuit comprising parallel

164   conductive pathways, the greatest change in film conductance is expected when the

165   largest conductive pathway is formed or removed. Accordingly, the rate of change

166   in film conductance with respect to temperature $\partial G \equiv \frac{d}{dT} R^{-1}$ (solid curves in Fig.

167   2b, obtained from *ex situ* resistance measurements) reaches a maximum value when

168   the largest conducting pathway (spanning the film electrodes) is broken up. The

169   comparison between A_{max} and ∂G (Fig. 2b) shows that percolation thresholds

170   identified both *in* and *ex situ* agree to within 1 K and percolation occurs at 168 K

171   (174 K) upon cooling (warming).

172   Having substantiated a nano-scale classification of metal and insulator, our

173   binary images therefore estimate relative areal fractions of insulating and metallic

174   phases. Moreover, *ex situ* XRD measurements of the same V_2O_3 film reveal relative

175   intensities of corundum and monoclinic diffraction peaks (Methods), allowing

176   assessment of constituent structural phase fractions (Fig. 2c). Fig. 2d compares the

177   thermometry-calibrated (see SI) metallic fraction (symbols) obtained by nano-IR to

178   the corundum fraction (solid curves) obtained by XRD, revealing a surprising 6K

179   thermal offset between electronic and structural transitions. Consistent with the

180   percolation temperature identified *in* and *ex situ*, we find the metallic constituent is

181   about 60% at 168 K while cooling, whereas the occupation of the corundum phase

182   at this temperature remains ~25%, with an uncertainty of about 10%. This strongly

183   implies that some metallic regions exhibit the monoclinic structure. Correlative

184   nano-IR and XRD measurements thus provide the first strong evidence for

185   asynchronous electronic and structural transitions in a V_2O_3 film.

186

187   The distribution of insulator-metal transition temperatures (T_{IMT}) obtained

188   on the basis of our binary analysis is presented in Fig. 3a, with data from cooling and

189   warming consolidated together (after removing the relative 6K hysteresis). We

190   identify the marked peak of the distribution with a characteristic temperature T_E for

191   the electronic transition, equal to 164K (169K) for cooling (warming). The IMT

192   occurs with greatest spatial prevalence at this temperature, a full 10K below the

193   structural phase transition temperature T_{SPT}, where the SPT occurs most rapidly

194   (and where structural phases are observed at approximately 50% fraction). Fig. 3b

195   presents a phase diagram comprised of relevant phase fractions (PF) obtained from

196   our data, with electronic and structural transitions shown on orthogonal axes. Most

197   importantly, the temperature range for appearance of putative monoclinic metal

198   (MM) is denoted in proximity to T_E.

199   The most striking feature initially resolved by our images with decreasing

200   temperature is the formation of bi-directional stripes, suggesting an underlying

201   organizational principle that could further elucidate interplay between structural

202   and electronic transitions. To characterize growth of these stripes, we measure the

203   extent of orientational anisotropy presented by domain walls – the boundaries

204   between metal and insulator in our binarized images – as a function of temperature

205 (SI and Fig. S7). Fig. 3c shows that domain wall anisotropy is maximized 10K above

206 T_E, matching well the structural phase transition temperature T_{SPT}. Likewise, we

207 detect a pattern of topographic corrugations (Fig. 3e) emerging with the underlying

208 SPT (SI and fig. S8). Nanometer-scale surface buckling follows from the differential

209 unit cell volumes of coexisting structural domains [28,14] and its topographic detection

210 by our AFM broadly coincides in real-space with the striped electronic nano-texture

211 (Fig. 3d and fig. S9). By way of this buckling, irreversible damage to the film is

212 avoided amidst the SPT through some out-of-plane relief of accommodation strain.

213 The buckling pattern spatially correlates with our nano-IR images most strongly at

214 temperatures where the IMT and SPT overlap (SI and fig. S9). Moreover, this

215 striped nano-texture also exhibits periodicity that is best revealed through the *static*

216 *structure factor*, obtained as the spatial Fourier transform of the 2-dimensional

217 correlation function for phase coexistence, which we compute for each nano-IR

218 image (Methods) [6,29]. Panels in Fig. 3f present the structure factor amplitude at

219 three characteristic cooling temperatures: close to T_{SPT} (T_E+10K), above T_E (T_E+4K),

220 and below T_E (T_E-5K). Peaks in the structure factor are most distinct near T_{SPT}.

221 These quantify preferential wave-vectors for the formation of stripes, here spaced at

222 60° or 120° angular separations, explicitly revealing that 3-fold rotational symmetry

223 of the high-temperature corundum structure is broken by at least two monoclinic

224 twin configurations [30]. A third expected crystallographic twin is unobserved in our

225 images, likely due to elastic mismatch of this monoclinic twin with the sapphire

226 substrate.

227   Meanwhile, the average length scale associated with these wave-vectors

228   conveys the natural periodicity associated with phase coexistence in our film [31,32],

229   which we denote the structural correlation length ξ_{struct}. Fig. 4a presents a graphical

230   definition of ξ_{struct}, superimposed on one section of the correlation function obtained

231   perpendicular to stripes observed near T_{SPT} (fig. S10). As shown in Fig. 4b, ξ_{struct}

232   rises abruptly to a value of about 1.2 μm with a broad plateau centered also in the

233   temperature range identified by XRD with the SPT. The association of long-range

234   spatial correlations and striped texture nano-texture with T_{SPT} is unmistakable.

235   Indeed, a well-known real-space pattern of equilibrium structural phase coexistence

236   (SPC) can emerge spontaneously during a SPT, taking the form of a striped "tweed"

237   texture (Fig. 4c) to minimize elastic strain energies among structural domains and

238   the substrate [33,31,32,34]. Detailed studies of the sister compound VO_2 have revealed

239   similar real-space patterns of SPC tunable by temperature and by intrinsic or

240   extrinsic stress [35,28,36,37]. Therefore, observed temperature dependent anisotropy

241   and ξ_{struct} both suggest that electronic nano-texture observed in our images within

242   this stage of the transition is largely a consequence of the IMT "guided" by the

243   underlying SPT. Within this ~20K temperature window, lattice mismatch between

244   monoclinic and corundum domains results in long-range accommodation strain

245   whose real-space patterns imprint on the local electronic phase.

246   At the final stages of the transition, we meanwhile observe clues concerning

247   the character of low-temperature metallicity in our V_2O_3 film.   The

248   phenomenological Landau theory of phase transitions holds that a thermally

249   fluctuating balance between volumetric and surface free energies among competing

250   phases (attributable in the Mott transition to electronic degrees of freedom [25])

251   dictates the spatial extent of short-range correlations [38]. We denote this spatial scale

252   the electronic correlation length ξ_{elec}, and extract it at each temperature from the

253   central full-width at half maximum of the correlation function (Fig. 4a; see

254   Methods). Shown in Fig. 4e and 4f, ξ_{elec} quantifies the characteristic length scale for

255   locally correlated electronic domains, reaching a maximum (~400 nm) at T_E. The

256   growth and peak in ξ_{elec} reveals the tendency for metallic domains to form

257   "droplets" near T_E rather than stripes (Figs. 4f and 4i), and resembles the strong

258   temperature dependence of spatial correlations more characteristic of continuous

259   phase transitions, which can exhibit universal scaling near criticality [38,17]. Whereas

260   influence of the STP complicates unambiguous quantitative extraction of ξ_{elec} versus

261   T, throughout the transition we nevertheless observe robust critical scaling in the

262   temperature dependence of the largest electronic domain size $d_{max} \equiv \sqrt{A_{max}}$,

263   observed to scale as $\left|T - T_{perc}\right|^{-\upsilon}$ with $\upsilon = 0.96 \pm 0.07 \approx 1$ (Fig. 4d).   Noting that

264   metallic percolation extends predominantly from the largest metallic cluster, our

265   directly resolved scaling shows quantitative agreement with the scale invariant

266   nucleation site density inferred from area-averaged optical studies of V_2O_3 films

267   grown by the same method (Methods) [39].

268   Although we cannot rule out an origin for these critical behaviors prosaically

269   tied to disorder (*e.g.* the Anderson-Mott transition), it is noteworthy that our V_2O_3

270   film presents a metal-insulator transition among the cleanest (most abrupt) yet

271   reported. In the clean limit, whereas critical scaling behaviors are conventionally at

272   odds with a bulk first order transition, they might here be reconciled with

273 predictions for phase separation in the Hubbard model. Below the Mott transition

274 temperature, uniform band filling in the homogeneous state is proposed to become

275 unstable at fixed chemical potential μ, and the system phase-separates into regions

276 with distinct charge density n associated with the insulating state at half band-filling

277 and a slightly doped metallic state. [40] This charge disproportionation Δn is

278 theorized to reach a few percent upon decreasing temperature. Consequently, long-

279 ranged Coulomb interactions are expected to penalize macroscopic charge

280 imbalance, whereas positive surface tension favors few coexistent domains,

281 resulting in glassy electronic phase coexistence with droplets of characteristic size

282 $\xi_{\text{elec}} \sim (\frac{\sigma}{\Delta n^2})^{1/d}$ in a d-dimensional IMT [41,42]. Tied to growing Δn for temperatures

283 below T_{IMT} [40], *Coulomb frustration* intensifying away from the local transition

284 temperature could underlie our observation of metallic droplets persisting at

285 rapidly suppressed length scales amidst this IMT (Figs. 4d and e). We speculate the

286 behavior of $\xi_{\text{elec}}(T)$ might provide spatial sensitivity to $\Delta n(T)$ at experimentally

287 fixed chemical potential, a real-space window into the μ-n phase diagram for

288 coexistent phases of the transition.

289   We can confirm directly that the IMT proceeds by a first-order electronic

290 phase transition even among these low temperature metallic droplets. Enabled by

291 colocalized nano-imaging within our FOV, Fig. 4g presents characteristic transition

292 curves (σ vs. T) for *loci* of pixels that exhibit the same transition temperature T_{IMT}

293 upon cooling (associated spatial maps of T_{IMT} presented in fig. S11). Taking the

294 initial transition curve at T_{IMT}=176K for reference, Fig. 4h reveals a sharp first-order

295 discontinuity in σ for all T_{IMT}, and by implication, abrupt decrease in the free carrier

13

296   optical response.   Sir Neville Mott's idealization of this IMT predicted such

297   discontinuity on the basis of the long-range Coulomb interaction [8].   Even without

298   lattice coupling, studies of the Hubbard model including beyond nearest-neighbor

299   interactions have postulated a first-order Mott transition [43,9,40], consistent with our

300   observations among metallic droplets, upon cooling many of which have

301   presumably already undergone the structural transition.

302

303   Our observation of this low temperature metallic phase (Fig. 4i) aligns with

304   reports for the related correlated oxide VO_2 [15,22,16,14,29,44]. Whereas a transient or

305   pressure-induced MM has been observed even in VO_2 single-crystals [45,46], its more

306   robust appearance in extrinsically or epitaxially strained samples suggests a general

307   mechanism decoupling the IMT from the SPT. Studies of the semi-infinite Hubbard

308   model for example have predicted stable interfacial metallicity amidst a bulk Mott

309   insulating state [47]. Meanwhile, X-ray absorption studies of V_2O_3 have identified

310   inequivalent metallic states attained through purely thermal or pressure-driven

311   transitions [48] and have revealed a novel pressure-induced MM phase [13], perhaps

312   related to that detected here.

313   We propose that epitaxial strain and the consequent striped SPT nanotexture

314   may play a crucial role among films. Stabilization of an intermediate monoclinic

315   metal may demand a strain environment fostered by pervasive structural domain

316   walls, implicit within the striped nanotexture we resolve in this correlated insulator.

317   Indeed, a stabilized intermediate electronic state with attributes of the high-

318   temperature phase has already been observed at temperatures below the

319   magnetoresistive transition of manganite films, attributed likewise to the

320   accommodation strain of coexistent structural phases. [49] Consequently, we

321   speculate that a monoclinic metal may assist in strain relief at structural domain

322   boundaries. Moreover, growing Coulomb frustration below T_{IMT} may afford further

323   stability to an intermediary phase in our V_2O_3 film.

324   Associating the monoclinic metal with a strain-induced or Coulomb-

325   frustrated phase suggests novel real-space facets of the electronic (Mott) transition

326   in this correlated insulator, hitherto unexplored at this spatial resolution. Our study

327   reveals the rich impact of nanotextured inhomogeneity on the low temperature

328   insulator-metal transition in V_2O_3, affirming that exotically rich behaviors can

329   underlie even this classic insulator-metal transition, moreover demanding

330   amendments to the bulk V_2O_3 phase diagram for epitaxial structures [17,8]. Low-

331   temperature nano-spectroscopic probes and X-ray magnetic imaging will be

332   imperative to further elucidate the electronic character of exotic phases emerging

333   amidst the insulator-metal transition in V_2O_3 and other correlated oxides.

334

338

339 **Author Contributions:**

340   S. Wang and J. G. Ramirez grew the V_2O_3 film. A. S. McLeod and E. van

341   Heumen performed nano-IR measurements on the film, whereas J. G. Ramirez

342   and T. Saerbeck performend x-ray diffraction and *ex situ* resistance

343   measurements on the film. A. S. McLeod, E. van Heumen, M. Goldflam, L.

344   Anderegg, and P. Kelly developed the nano-IR instrumentation. All authors

345   prepared the manuscript.

Methods

V$_2$O$_3$ Films

The V$_2$O$_3$ film studied in this work was epitaxially grown on (012)-plane sapphire substrate by RF magnetron sputtering from a V$_2$O$_3$ target (1.5" diameter, > 99.7%, ACI Alloys, Inc.). The samples are prepared in a high vacuum system with a base pressure of 1×10^{-7} Torr. The substrate temperature was kept at 750°C during the deposition. 4 mTorr ultrahigh purity (99.999%) Ar and 100 W RF power were used for the deposition of V$_2$O$_3$. These conditions yield a deposition rate of 0.67 Å/s. Based on X-ray diffraction characterization of the film, compressive strain from lattice mismatch between hexagonal lattice constants for room temperature sapphire and V$_2$O$_3$, combined with stress relief by film buckling and granularity, induces lattice expansion along the film c-axis and a concomitant increase in the c/a ratio relative to bulk crystals. Previous studies of sapphire-grown V$_2$O$_3$ films have equated this expansion with tensile hydrostatic chemical pressure attainable through chromium doping, affecting a putative decrease in bandwidth and increase in the Mott transition temperature [50]. Indeed, the transition temperature for our film is as much as 16K higher than for bulk crystalline V$_2$O$_3$. Notably, previous similarly grown films displayed characteristics similar to the best available single crystal samples.

Determination of structural phase fractions by X-ray diffraction

We have determined the SPT temperature and the crystallographic phase fraction in our film by performing temperature-dependent X-ray diffraction (XRD)

367   measurements. We measured the out-of-plane XRD of the rhombohedral (012) peak

368   shifts from $2\theta = 24.30°$ above the SPT (300 K) to the monoclinic (011) $2\theta = 24.05°$

369   below it (100 K). The peaks were then fitted with two Gaussian curves; keeping

370   fixed the 2θ values of the low and high temperature phases. The area under each

371   Gaussian was normalized to the total area and the percentage volume fraction of

372   each phase was thus obtained. The SPT temperature is obtained at the temperature

373   at which both phases are equally populated.

374   **Correlation Analysis**

375   Informally, the correlation function $g(\delta\vec{r})$ of an image $I(\vec{r})$ (evaluated at lateral

376   positions $\vec{r}$) expresses the level of statistical similarity between image features

377   separated by a displacement $\delta\vec{r}$. The correlation function is formally given by [38]:

378    $$g(\delta\vec{r}) = \langle \delta I(\vec{r}), \delta I(\vec{r} + \delta\vec{r}) \rangle = \int d^2\vec{r}\, [I(\vec{r}) - \langle I(\vec{r}) \rangle]\, [I(\vec{r} + \delta\vec{r}) - \langle I(\vec{r} + \delta\vec{r}) \rangle]. \quad (1)$$

379   Here $\langle \cdots \rangle$ indicates an areal average of the enclosed value. Appearance of the mean

380   value $\langle I(\vec{r}) \rangle$ in Eq. (1) reflects that only image inhomogeneities ("features") are

381   relevant for the characterization of spatial correlations. Eq. (1) was used to

382   compute the correlation function for each nano-IR image across the insulator-metal

383   transition of our V_2O_3 film. Each correlation function was normalized to unity at

384    $\delta\vec{r} = \vec{0}$, taken by construction to indicate 100% correlation.

385   The correlation function is known to reveal intrinsic periodicities more clearly

386   within noisy data than would be possible to identify through direct inspection alone.

387   We leverage this feature to identify periodicity in our nano-IR images, whose mean

388   length scale we identify as ξ_{struct}.   Meanwhile, the rotational average of the

389   correlation function (yielding $g(r)$, evaluated at displacement magnitude r alone)

390   was used to identify ξ_{elec} according to its central full-width at half-maximum.   This

391   correlation length reflects the typical scale for statistical correlations to locally

392   decay by e^{-1} and corresponds intuitively with the average dimension of

393   characteristic image inhomogeneities.   In our case these comprise droplets of the

394   minority electronic phase – whether insulating in character above the percolation

395   temperature, or metallic below.   The "divergent" character of ξ_{elec} revealed by our

396   correlation analysis and the thermal scaling of largest electronic cluster sizes both

397   qualitatively match the phenomenology of Landau theory for scale-invariant spatial

398   fluctuations proximate to a *continuous* phase transition, or alternatively a scenario

399   of temperature-dependent Coulomb frustration. [42,41,40]

400   References

1. Dagotto, E., Complexity in strongly correlated electronic systems. *Science* **309**, 257 (2005).

2. Tranquada, J. M., Sternlieb, B. J., Axe, J. D., Nakamura, Y. & Uchida, S., Evidence for stripe correlations of spins and holes in copper oxide superconductors. *Nature* **375**, 561-563 (1995).

3. Lawler, M. J. *et al.*, states, Intra-unit-cell electronic nematicity of the high-Tc copper-oxide pseudogap. *Nature* **466**, 347-351 (2010).

4. Uehara, M., Mori, S., Chen, C. H. & Cheong, S. W., Percolative phase separation underlies colossal magnetoresistance in mixed-valent manganites. *Nature* **399**, 560-563 (1999).

5. Ahn, K. H., Lookman, T. & Bishop, A. R., Strain-induced metal-insulator phase coexistence in perovskite manganites. *Nature* **428**, 401-404 (2004).

6. Lai, K. *et al.*, Mesoscopic Percolating Resistance Network in a Strained Manganite Thin Film. *Science* **329**, 190-193 (2010).

7. Knoll, B. & Keilmann, F., Near-Field probing of vibrational absorption for chemical microscopy. *Nature* **399**, 134-137 (1999).

8. Imada, M., Fujimori, A. & Tokura, Y., Metal-insulator transitions. *Rev. Mod. Phys.* **70**, 1039 (1998).

9. Rozenberg, M. J. *et al.*, Optical Conductivity in Mott-Hubbard Systems. *Physical Review Letters* **75**, 1 (1995).

10. Stewart, M. K. *et al.*, Insulator-to-metal transition and correlated metallic state of V2O3 investigated by optical spectroscopy. *Phys. Rev. B* **85**, 205113 (2012).

11. Lupi, S. *et al.*, A microscopic view on the Mott transition in Chromium-doped V2O3. *Nature Comm.* **1**, 105 (2010).

12. Liu, M. K. *et al.*, Photoinduced Phase Transitions by Time-Resolved Far-Infrared Spectroscopy in V2O3. *Phys. Rev. Lett.* **107**, 066403 (2011).

13. Ding, Y. *et al.*, Novel High-Pressure Monoclinic Metallic Phase of V2O3. *Phys. Rev. Lett.* **112**, 056401 (2014).

14. Liu, M. K. *et al.*, Anisotropic Electronic State via Spontaneous Phase Separation in Strained Vanadium Dioxide Films. *Phys. Rev. Lett.* **111**, 096602 (2013).

15. Kim, B.-J. *et al.*, Micrometer x-ray diffraction study of VO2 films: Separation between metal-insulator transition and structural phase transition. *Phys. Rev. B* **77**, 235401 (2008).

16. Tao, Z. *et al.*, Decoupling of Structural and Electronic Phase Transitions in VO2. *Phys. Rev. Lett.* **109**, 166406 (2012).

17. Limelette, P. *et al.*, Universality and Critical Behavior at the Mott Transition. *Science* **302**, 89-92 (2003).

18. Guénon, S. *et al.*, Electrical breakdown in a V2O3 device at the insulator-to-metal transition. *Europhysics Letters* **101**, 57003 (2013).

19. Gebhard, F., *The Mott Metal-Insulator Transition: Models and Methods* (Springer Tracts in Modern Physics, Berlin, 1997).

20. Atkin, J. M., Berweger, S., Jones, A. C. & Raschke, M. B., Nano-optical imaging and spectroscopy of order, phases, and domains in complex solids. *Advances in Physics* **61** (6), 745-842 (2012).

21. Yang, H. U., Hevestreit, E., Josberger, E. E. & Raschke, M. B., A cryogenic scattering-type scanning near-field optical microscope. *Rev. Sci. Instrum.* **84**, 023701 (2013).

22. Qazilbash, M. M. *et al.*, Mott Transition in VO2 Revealed by Infrared Spectroscopy and Nano-Imaging. *Science* **318**, 1750-1753 (2007).

23. Baldassarre, L. *et al.*, Quasiparticle evolution and pseudogap formation in V2O3: An infrared spectroscopy study. *Phys. Rev. B* **77**, 113107 (2008).

24. Qazilbash, M. M. *et al.*, Infrared spectroscopy and nano-imaging of the insulator-to-metal transition in vanadium dioxide. *Phys. Rev. B* **79**, 075107 (2009).

25. Georges, A., Krauth, W. & Rozenberg, M. J., Dynamical mean-field theory of strongly correlated fermion systems and the limit of infinite dimensions. *Rev. Mode. Phys.* **68**, 3 (1996).

26. Park, H., Haule, K. & Kotliar, G., Cluster dynamical mean field theory of the Mott transition. *Phys. Rev. Lett.* **101**, 186403 (2008).

27. Hillenbrand, R. & Keilmann, F., Complex optical constants on a subwavelength scale. *Phys. Rev. Lett.* **85** (14), 3029-3032 (2000).

28. Tselev, A. *et al.*, Interplay between Ferroelastic and Metal-Insulator Phase Transitions in Strained Quasi-Two-Dimensional VO2 Nanoplatelets. *Nano Letters* **10**, 2003-2011 (2010).

29. Laverock, J. *et al.*, Direct observation of decoupled structural and electronic transitions and an ambient pressure monocliniclike metallic phase of VO2. *Phys. Rev. Lett.* **113**, 216402 (2014).

30. Roytburd, A. L., Thermodynamics of polydomain heterostructures I. Effect of macrostresses. *Appl. Phys. Lett.* **83**, 228 (1998).

31. Gao, Y. F., Lu, W. & Suo, Z., A mesophase transition in a binary monolayer on a solid surface. *Aca Materialia* **50**, 2297-2308 (2002).

32. Bratkovsky, A. M., Marais, S. C., Heine, V. & Salje, E. K. H., The theory of fluctuations and texture embryos in structural phase transitions mediated by strain. *J. of Phys.: Condensed Matter* **6**, 3679-3696 (1994).

33. Seul, M. & Andelman, D., Domain Shapes and Patterns: The Phenomenology of Modulated Phases. *Science* **267**, 476-483 (1995).

34. Marais, S., Phenomena Due to Strain Coupling in Phase Transitions. *Phys. Rev. Lett.* **66**, 2480-2483 (1991).

35. Cao, J. *et al.*, Strain engineering and one-dimensional organization of metal–insulator domains in single-crystal vanadium dioxide beams. *Nat. Nanotechnology* **4**, 732-737 (2009).

36. Wu, J. *et al.*, Strain-Induced Self Organization of Metal–Insulator Domains in

Single-Crystalline VO2 Nanobeams. *Nano Letters* **6** (10), 2313-2317 (2006).

37. Jones, A. C., Berweger, S., Wei, J., Cobden, D. & Raschke, M. B., Nano-optical Investigations of the Metal-Insulator Phase Behavior of Individual VO2 Microcrystals. *Nano Letters* **10**, 1574-1581 (2010).

38. Kadanoff, L. P. *et al.*, Static Phenomena Near Critical Points: Theory and Experiment. *Rev. Mod. Phys.* **39** (2), 395-431 (1967).

39. Abreu, E. *et al.*, Dynamic conductivity scaling in photoexcited V2O3 thin films. *Phys. Rev. B* **92** (085130) (2015).

40. Macridin, A., Jarrell, M. & Maier, T., Phase separation in the Hubbard model using the dynamical cluster approximation. *Phys. Rev. B* **74**, 085104 (2006).

41. Ortix, C., Lorenzana, J. & Di Castro, C., Universality classes for Coulomb frustrated phase separation. *Physica B* **404**, 499-502 (2009).

42. Yee, C.-H. & Balents, L., Phase Separation in Doped Mott Insulators. *Phys. Rev. X* **5**, 021007 (2015).

43. Chitra, R. & Kotliar, G., Effect of Long Range Coulomb Interactions on the Mott Transition. *Phys. Rev. Lett.* **84** (16), 3678-3681 (2000).

44. Ramirez, J.-G., Sharoni, A., Dubi, Y., Gomez, M. E. & Schuller, I. K., First-rder reversal curve measurements of the metal-insulator transition in VO2: Signatures of persistent metallic domains. *Phys. Rev. B* **79**, 235110 (2009).

45. Baum, P., Yang, D.-S. & Zewail, A. H., 4D Visualization of Transitional Structures in Phase Transformations by Electron Diffraction. *Science* **318**, 788 (2007).

46. Arcangeletti, E. *et al.*, Evidence of a Pressure-Induced Metallization process in Monoclinic VO2. *Phys. Rev. Lett.* **98**, 196406 (2007).

47. Potthoff, M. & Nolting, W., Metallic surface of a Mott insulator–Mott insulating surface of a metal. *Phys. Rev. B* **60** (11), 7834 (1999).

48. Rodolakis, F. *et al.*, Inequivalent Routes across the Mott Transition in V2O3 Explored by X-Ray Absorption. *Phys. Rev. Lett.* **104**, 047401 (2010).

49. Podzorov, V., Kim, B. G., Kiryukhin, V., Gershenson, M. E. & Cheong, S.-W., Martensitic accommodation strain and the metal-insulator transition in manganites. *Physical Review B Rapid Communications* **64** (140406) (2001).

50. Allimi, B. S. *et al.*, Resistivity of V2O3 thin films deposited on a-plane (110) and c-plane (001) sapphire by pulsed laser deposition. *Appl. Phys. Lett.* **92**, 202105 (2008).

402

403
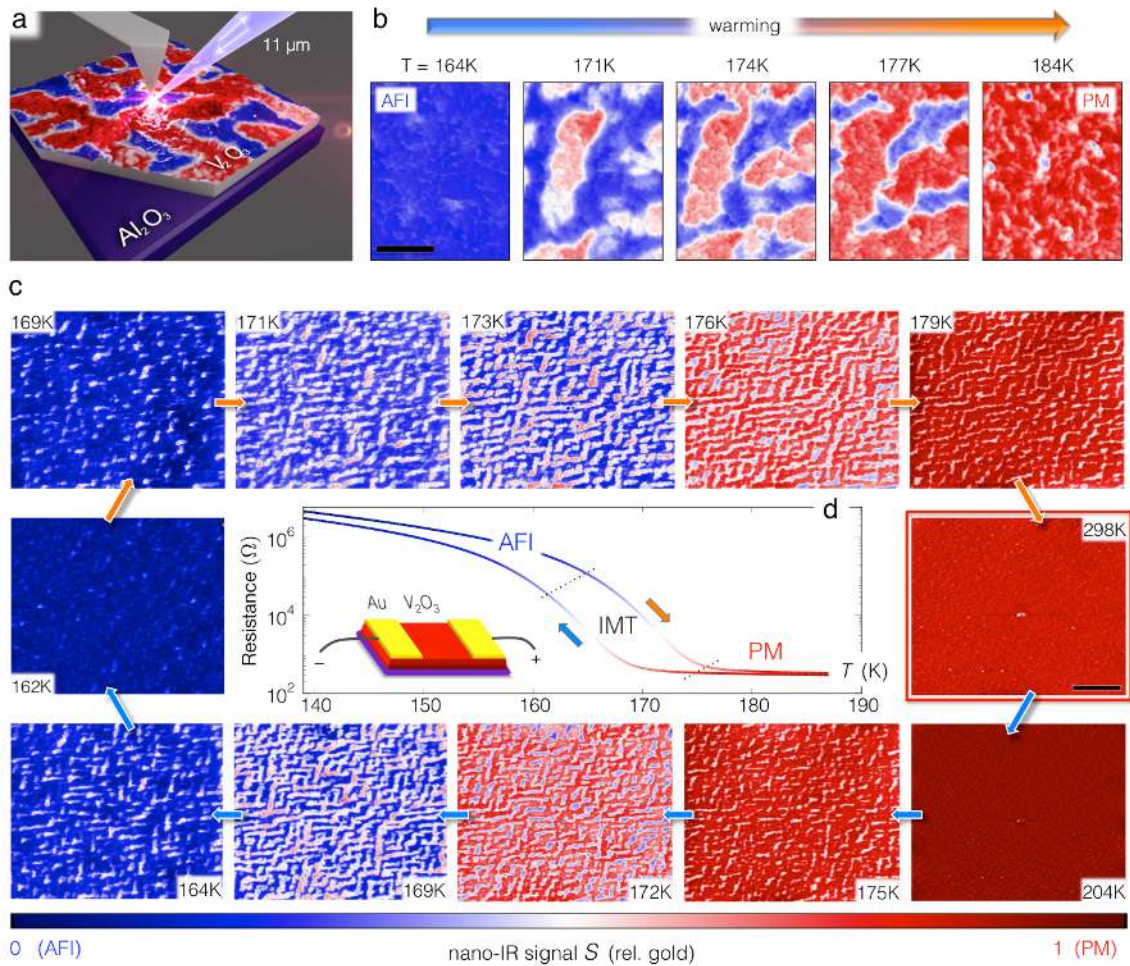
Figure 1 | nano-IR imaging of the low temperature Mott transition in V_2O_3. a) Schematic depiction of near-field microscopy of phase coexistence in a V_2O_3 thin film; nano-IR signal S superimposed on film topography at 171K (cooling). b) High-resolution co-localized near-field images of coexisting phases evolving upon warming the film from the antiferromagnetic insulator (AFI) to paramagnetic metal (PM) phase; 1 micron scale bar; color scale as in c). c) Large-area co-localized nano-IR images of the electronic phase transition upon cooling (blue arrows) and warming (orange arrows); 5 microns scale bar. The color scale (bottom) distinguishes metallic from insulating regions. d) Resistance of the film versus

415   temperature upon cooling (blue arrow) and warming (orange arrow); dashed lines

416   demarcate the temperature range of phase-coexistence in the insulator-to-metal

417   transition (IMT). Inset: schematic arrangement of gold pads on the film surface

418   used as in-situ transport electrodes and for quantitative normalization of near-field

419   images.
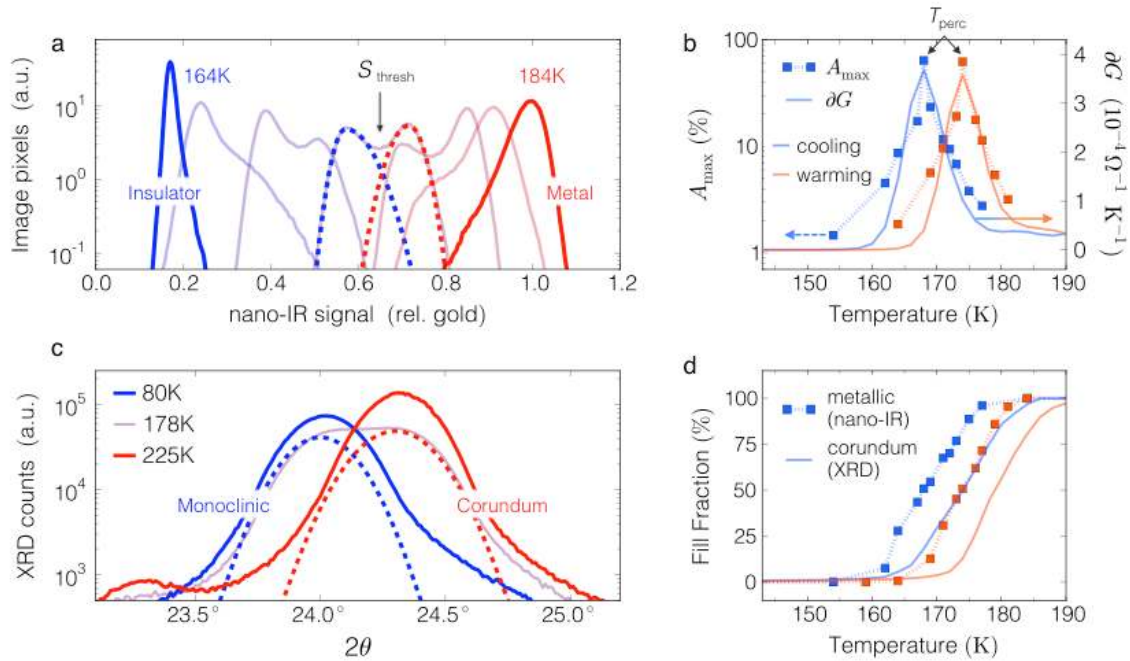
Figure 2 | Binary analysis of phase populations. a) Histogram representation of nano-IR signals (*viz.* levels of free carrier optical response) recorded from the V_2O_3 film at several temperatures upon warming from 164K to 184K relative to an ideal metal (gold). An example fit to the distribution at 173K by two asymmetric normal distributions reveals insulating (dashed blue) and metallic (dashed red) populations evolving with temperature and demarcated by a threshold nano-IR signal level (S_{thresh}); note vertical log scale. b) Comparison of the largest electronic cluster size observed by nano-IR imaging (A_{max}) against changes in film transport conductance per unit temperature ∂G for both cooling and warming; both metrics identify a coincident percolation temperature T_{perc}. c) Bimodal decomposition of diffraction peaks measured by X-ray diffraction (XRD) admits measurement of structural phase fractions (Methods). d) Thermometry-calibrated comparison of phase fractions for

434   the metallic phase identified by nano-IR imaging against those for the high-

435   temperature structural phase (corundum) identified by XRD; an anomalous thermal

436   offset suggests persistent metallicity in the monoclinic structure.

437

438

439
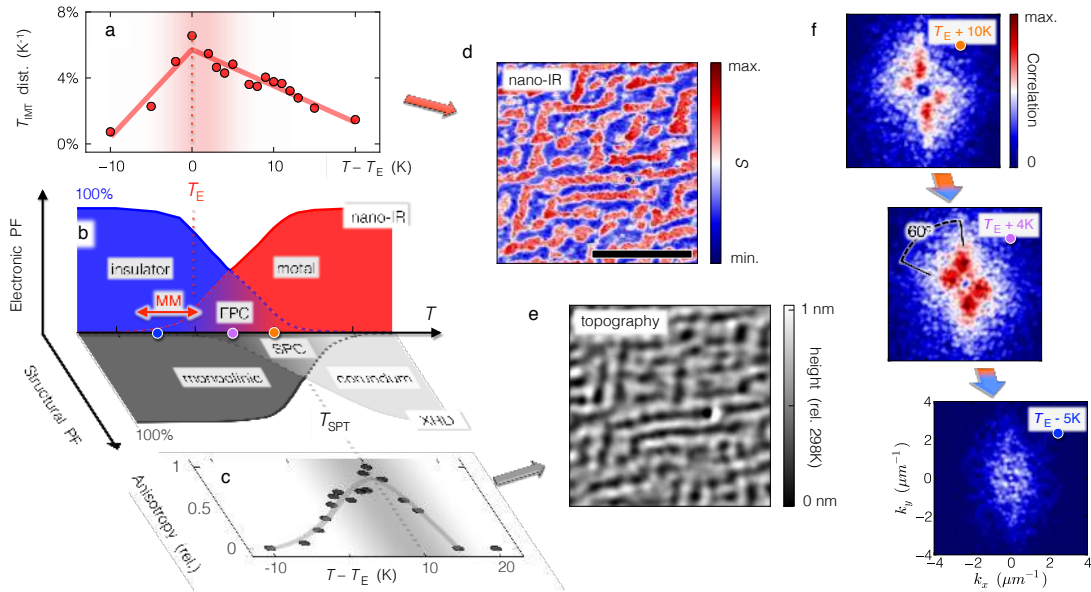
Figure 3 | Phase diagram of electronic and structural phases in thin-film V_2O_3.

a) Distribution of insulator-metal transition temperatures T_{IMT} obtained as the fraction of observed pixels to transition per degree K; data from cooling and warming together. The peak in the transition indicates the most likely transition temperature, denoted T_E. b) Phase diagram presenting T-dependent fill fractions (FF) for electronic and structural phases (orthogonal axes) measured by nano-IR imaging and X-ray diffraction (XRD). EPC = electronic phase coexistence; SPT = structural phase coexistence; MM = monoclinic metal. c) Directional anisotropy of electronic domain walls versus temperature as obtained from a binary insulator-metal classification of nano-IR image pixels; anisotropy maximizes abruptly at the structural phase transition temperature T_{SPT}, associating electronic anisotropy with "guiding" by the SPT. d) Subset of nano-IR image at T_E+4K (warming) compared

452   with e) relative topographic corrugations detected simultaneously by AFM. f) Static

453   structure factor (see text) of EPC measured near T_{SPT}, above T_E, and below T_E,

454   revealing preferred structural wave-vectors emerging at 60° lateral separations;

455   temperatures indicated by dots on the phase diagram panel b).
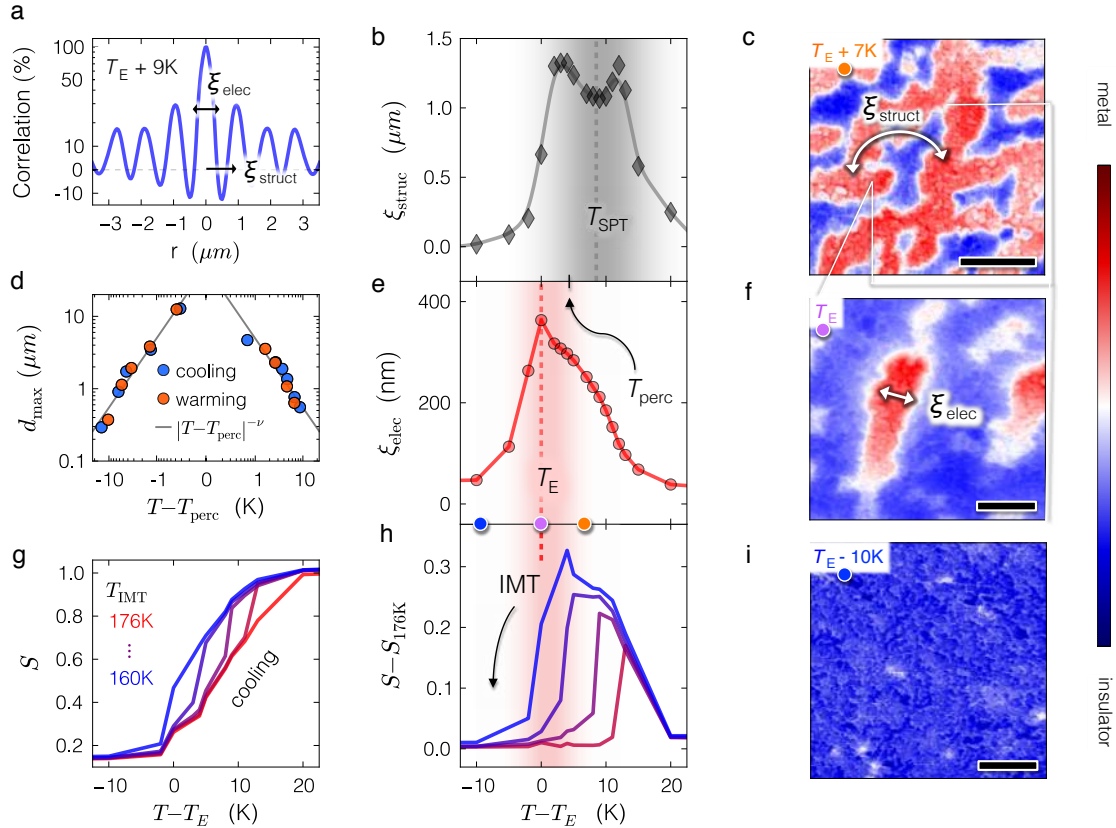
Figure 4 | Characteristics of persistent metallicity. a) Trace from the image correlation function obtained 9K above T_E, perpendicular to the direction of stripes; relevant correlation lengths are indicated. b) The structural correlation length associated with periodic correlations; ξ_{struct} plateaus at T_{SPT} and originates from structural phase coexistence. c,f,i) Acquisition temperatures for nano-IR images indicated by colored dots in panel e). c) Indication of ξ_{struct} associated with real-space stripe periodicity; scale bar: 2 microns. d) Scale invariance of the largest electronic domain size d_{max}, fitting a power law with critical exponent $\nu \approx 1$ close to the percolation threshold temperature T_{perc}. e) The electronic correlation length associated with short-range correlations; ξ_{elec} peaks abruptly at T_E. f) Indication of

468   ξ_{elec} associated with the characteristic size of metallic droplets; field of view is a

469   subset of panel c); scale bar: 1 micron. g) Average transition curves (nano-IR signal

470   σ vs. T) acquired from pixels exhibiting insulator-metal transition temperatures

471   T_{IMT}=176K to 160K upon cooling. h) Curves from g) after referencing to T_{IMT}=176K,

472   revealing a first-order discontinuity in σ down to T_{IMT}=160K. i) Putative monoclinic

473   metallic matches persisting even 10K below T_E, and further yet below T_{SPT}; scale

474   bar: 1 micron.